

A Trust-Guided Approach to MR Image Reconstruction with Side Information

Arda Atalık, Sumit Chopra, and Daniel K. Sodickson

Abstract—Reducing MRI scan times can improve patient care and lower healthcare costs. Many acceleration methods are designed to reconstruct diagnostic-quality images from limited sets of acquired k -space data. This task can be framed as a linear inverse problem (LIP), where, as a result of undersampling, the forward operator may become rank-deficient or exhibit small singular values. This results in ambiguities in reconstruction, in which multiple generally incorrect or non-diagnostic images can map to the same acquired data. To address such ambiguities, it is crucial to incorporate prior knowledge, for example in the form of regularization. Another form of prior knowledge less commonly used in medical imaging is contextual *side information* garnered from other sources than the current acquisition. Here, we propose the *Trust-Guided Variational Network* (TGVN), a novel end-to-end deep learning framework that effectively integrates side information into LIPs. TGVN eliminates undesirable solutions from the *ambiguous space* of the forward operator while remaining faithful to the acquired data. We demonstrate its effectiveness in multi-coil, multi-contrast MR image reconstruction, where incomplete or low-quality measurements from one contrast are used as side information to reconstruct high-quality images of another contrast from heavily under-sampled data. Our method is robust across different contrasts, anatomies, and field strengths. Compared to baselines that also utilize side information, TGVN achieves superior image quality at challenging under-sampling levels, drastically speeding up acquisition while minimizing hallucinations. Our approach is also versatile enough to incorporate many different types of side information (including previous scans or even text) into any LIP.

Index Terms—Deep learning, linear inverse problems, MR image reconstruction, side information, variational network

I. INTRODUCTION

This work was supported in part by the National Institute of Biomedical Imaging and Bioengineering (NIH P41 EB017183) and the National Science Foundation (NSF Award 1922658). Not in connection with this work, Dr. Sodickson receives fees and holds stock options as a scientific advisor for Ezra, and receives royalties from a patent on deep learning-based image reconstruction licensed by Siemens Healthineers.

Arda Atalık is with the NYU Center for Data Science, and also with the Center for Advanced Imaging Innovation and Research (CAI²R) and the Bernard and Irene Schwartz Center for Biomedical Imaging, Department of Radiology, NYU Grossman School of Medicine. (e-mail: Arda.Atalik@nyu.edu)

Sumit Chopra is with the Courant Institute of Mathematical Sciences, and also with the Bernard and Irene Schwartz Center for Biomedical Imaging, Department of Radiology, NYU Grossman School of Medicine. (e-mail: Sumit.Chopra@nyulangone.org)

Daniel K. Sodickson is with the Center for Advanced Imaging Innovation and Research (CAI²R) and the Bernard and Irene Schwartz Center for Biomedical Imaging, Department of Radiology, NYU Grossman School of Medicine. (e-mail: Daniel.Sodickson@nyulangone.org)

MAGNETIC Resonance Imaging (MRI) is a mainstay of medical diagnostic imaging, thanks to its flexibility, its rich information content, and its excellent soft-tissue contrast. An MR scanner collects measurements in frequency space (a.k.a., k -space) that encode the body’s response to applied electromagnetic fields, with multiple receiver coils capturing distinct views modulated by their individual sensitivities. These measurements are then used to reconstruct high-fidelity diagnostic quality images. The problem of image reconstruction from multi-coil k -space data can be formulated as a Linear Inverse Problem (LIP), where the objective is to deduce an accurate representation of structures in an object of interest (i.e., an image) from the observed measurements. The term “linear” refers to the linear relationship between the observed measurements and the object of interest, which is defined by a known process called the *forward operator*.

Despite MRI’s superior diagnostic capabilities, it is comparatively time-consuming and costly, which limits its overall accessibility. Reducing the time it takes to acquire an MR scan is an important practical problem that can improve patient care, limit patient discomfort, reduce costs, and improve accessibility of this imaging modality. One way to reduce scan time is to acquire a smaller number of k -space measurements. The challenge then becomes how to reconstruct high-quality images from limited data. Undersampling in k -space renders the underlying LIP ill-posed or ill-conditioned, because the forward operator becomes either rank deficient or ill-conditioned, leading to ambiguities in the reconstruction process: multiple solutions (most of them not representing key anatomic and clinical information accurately) can map to the same set of acquired data.

These ambiguities are generally resolved through some form of regularization using prior knowledge about the properties of desirable solutions. Researchers have proposed various solutions, including compressed-sensing-based methods [1] and priors learned from exemplary data or directly from the measurements themselves [2], [3]. Recent advances in machine learning, and particularly deep learning techniques, have markedly improved the ability to tackle ill-posed or ill-conditioned problems. Notable early examples include the Variational Network (VarNet) approach [4], [5], the Model-Based Deep Learning (MoDL) approach [6], and the FISTA-Net approach [7], all of which integrate traditional optimization techniques with deep neural networks to achieve robust and efficient solutions in high-dimensional spaces. More recently, researchers have proposed generative models for reconstructing high-quality images from incomplete data [8]–

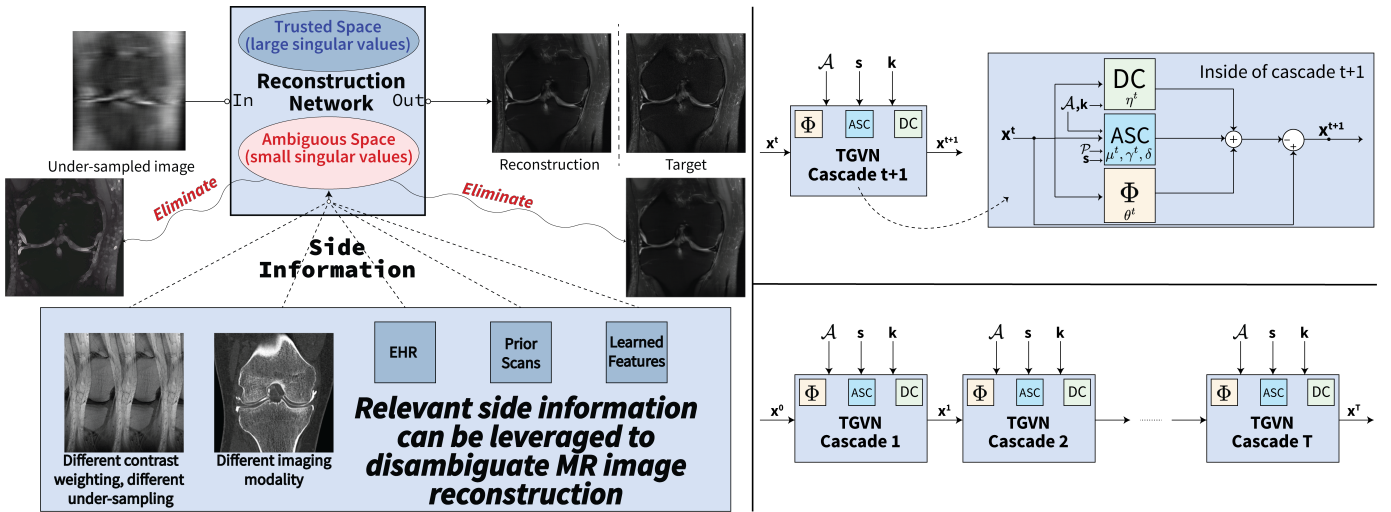


Fig. 1: TGVN reconstruction with side information. Left: High-level illustration of trust-guided disambiguation of solutions to an image reconstruction inverse problem. Upper right: A single TGVN cascade element and its component operations consisting of data consistency (DC), ambiguous space consistency (ASC) and refinement (Φ). The novelty of our work lies in the inclusion of an ASC module which incorporates the side information (s) through a projection (\mathcal{P}) onto the ambiguous space of the forward operator to further disambiguate the reconstruction. Lower right: A full TGVN consisting of T cascade elements connected in series.

[10], and a rapidly-expanding portfolio of deep-learning-based image reconstruction methods is currently under development. In all of these cases, performance at high acceleration levels is limited by the quantity of useful information that can reliably be derived about general distributions of desirable solutions. The extent to which such general information can correctly disambiguate particular solutions is also limited.

Another approach to eliminating degenerate solutions to ill-posed or ill-conditioned LIPs involves leveraging additional contextual information (a.k.a., *relevant side information*). While side information may also be incorporated via regularizers or constraints in the objective function of an optimization problem [11]–[16], it differs from population-based regularization in that it can be specific to the particular solution of interest. The nature of such side information is problem-dependent, and in many real-world scenarios it is readily available. Relevant side information can take multiple forms, including images, text, or other types of structured data. In MR image reconstruction, for instance, the side information could be data associated with prior scans of the same patient. It could also be data gathered during the same scan, such as images obtained using an imaging pulse sequence with a different underlying contrast from the target pulse sequence. (Note that reconstruction with different-contrast side information, also known as *conditional reconstruction*, refers to reconstructing only the target contrast while exploiting information from other contrasts. This approach differs from both single-contrast and joint multi-contrast reconstruction, though joint conditional reconstruction may also be leveraged for multi-contrast reconstruction.) In more general settings, the side information need not be derived from the same imaging modality, nor does it need to be image-based; it could be textual (e.g., clinical notes and medical history), audio, or even

encoded features or representations learned from other related tasks or from foundation models.

Contributions: In this work, we propose a novel, end-to-end trainable deep learning method that reliably integrates side information to solve LIPs, as illustrated in Fig. 1. Our method, called the **Trust-Guided Variational Network (TGVN)**, uses the side information to disambiguate the subspace spanned by the trailing right singular vectors of the forward operator of an LIP (i.e., the right singular vectors corresponding to small singular values). Specifically, we introduce a learnable squared Euclidean distance constraint, termed the *ambiguous space consistency* constraint, into the regularized least-squares reconstruction formulation of the LIP to eliminate undesirable solutions from the ambiguous space of the forward operator. This *ambiguous space consistency* constraint can be seamlessly integrated into any deep unrolled network. Our approach can be trained end-to-end with full supervision to maximize a similarity metric between the reconstructed and the ground truth image, requiring minimal modifications to integrate the constraint. By incorporating additional contextual data, our approach effectively reduces the ambiguities inherent in inverse problems, leading to more accurate and reliable solutions even when the measurements are exceedingly sparse. We demonstrate the effectiveness of our method in the challenging domain of multi-coil, multi-contrast MR image reconstruction, where incomplete or low-quality measurements from complementary contrast weighting are used as side information to reconstruct images with a different target contrast from exceedingly small quantities of k -space measurements (on the order of $20\times$ undersampling in a single phase-encoding direction) across different anatomies and field strengths. Compared to recently proposed machine learning-based solutions, our method leverages side information efficiently by focusing on the ambiguous solution space while maintaining consistency

with the acquired measurements, and achieves statistically significant improvements in reconstruction performance, highlighting the advantage of integrating additional context. To summarize:

- We propose a novel method called the **Trust-Guided Variational Network (TGVN)** that leverages side information to reliably solve ill-posed or ill-conditioned LIPs.
- We demonstrate the effectiveness of TGVN in multi-coil multi-contrast MR image reconstruction, using incomplete or low-quality measurements from complementary contrast weighting as side information.
- We demonstrate the robustness of our method by showing its efficacy for different contrasts across multiple anatomies and multiple field strengths.
- We show that TGVN leverages side information more efficiently than other recent ML-based solutions, achieving statistically significant improvements in image reconstruction performance and pushing the boundaries of current techniques in medical imaging and beyond.

We will release our code at github.com/sodicksonlab/TGVN to facilitate future research.

II. BACKGROUND

A. Multi-Coil MR Image Acquisition

In MR imaging, measurements are acquired in the spatial frequency (a.k.a., k -space) domain, and the measurements are related to the estimated MR image through the linear forward operator \mathcal{A} . These measurements may be grouped into a complex-valued vector \mathbf{k} , and the elements of \mathbf{k} represent Fourier coefficients of the structure of the continuous object being imaged. Specifically, we define a discrete estimated MR image \mathbf{x} , such that $\tilde{\mathbf{k}} = \mathcal{F}(\mathbf{x}) + \epsilon$, where ϵ is complex Gaussian noise and \mathcal{F} denotes the Fourier transform operator. The vector $\mathbf{x} \in \mathbb{C}^{MN}$ is a complex vector of size MN , where M and N are pixel dimensions of the two-dimensional image being sought.

In parallel imaging (PI), the scanner captures multiple views of the anatomy modulated by the sensitivities S_i of the receiver coils, which can be represented by diagonal matrices $\tilde{S}_i \in \mathbb{C}^{MN \times MN}$. In this case the relationship becomes $\tilde{\mathbf{k}}_i = \mathcal{F}(S_i \mathbf{x}) + \epsilon_i$, for each $i \in \{1, 2, \dots, N_c\}$, where N_c denotes the number of coils. To simplify notation, we aggregate the k -space data from all coils into a single tensor $\mathbf{k} = (\mathbf{k}_1, \dots, \mathbf{k}_{N_c})$ and define the *expand* operator (\mathcal{E}) which maps the complex image to multi-coil k -space. That is, $\mathcal{E} : \mathbf{x} \mapsto (\mathcal{F}(S_1 \mathbf{x}), \dots, \mathcal{F}(S_{N_c} \mathbf{x}))$. To accelerate MR acquisition, fewer k -space samples are acquired, which we denote by a binary diagonal mask matrix $\mathcal{M} \in \{0, 1\}^{MN \times MN}$, of size $MN \times MN$, whose diagonal element is set to 1 only if the corresponding measurement was acquired. Otherwise, it is set to 0. Thus, the set of under-sampled k -space measurements can be denoted as $\mathbf{k} \triangleq \mathcal{M}\tilde{\mathbf{k}} = (\mathcal{M}\tilde{\mathbf{k}}_1, \dots, \mathcal{M}\tilde{\mathbf{k}}_{N_c})$, and the forward operator \mathcal{A} —mapping the underlying image to the under-sampled and noisy k -space measurements—in multi-coil MR image acquisition is equal to $\mathcal{M} \circ \mathcal{E}$. That is,

$$\mathbf{k} = \mathcal{A}\mathbf{x} + \epsilon' = (\mathcal{M} \circ \mathcal{E})\mathbf{x} + \epsilon', \quad (1)$$

where ϵ' denotes the complex Gaussian noise in the under-sampled k -space measurements.

B. Deep Learning for Parallel MR Image Reconstruction

Given the forward operator \mathcal{A} and the k -space data \mathbf{k} , estimating \mathbf{x} is considered a *well-posed* problem if it meets the following three criteria (called the Hadamard conditions): 1) existence of a solution, 2) uniqueness of the solution, and 3) stability of the solution [17]. Accelerated parallel MR image reconstruction, however, like most real-world problems, is either *ill-posed*, failing to meet one or more of these criteria, or *ill-conditioned*, with small errors in the measurements leading to much larger errors in our image estimate \mathbf{x} . This is because the sparse set of measurements \mathbf{k} makes the above system of equations (1) either under-determined, with a potentially infinite set of solutions, or ill-conditioned, with a large yet finite condition number. When the measurement noise is Gaussian, the maximum likelihood estimate of a solution to (1) is given by $\hat{\mathbf{x}} = \arg \min_{\mathbf{x}} \frac{1}{2} \|\mathcal{A}\mathbf{x} - \mathbf{k}\|_2^2$. To address its ill-posed or ill-conditioned nature, the inverse problem is reformulated to impose additional constraints or requirements on the solution. By incorporating appropriate additional constraints, such as regularization, one can derive a reliable approximate solution. More formally, let $\Psi(\cdot)$ denote a regularization function that imposes certain constraints on the possible solutions \mathbf{x} . Then the optimization problem, (II-B), can be modified as:

$$\hat{\mathbf{x}} = \arg \min_{\mathbf{x}} \frac{1}{2} \|\mathcal{A}\mathbf{x} - \mathbf{k}\|_2^2 + \Psi(\mathbf{x}). \quad (2)$$

In deep-learning based unrolled networks, such as the End-to-end Variational Network (E2E-VarNet) [5], one learns a regularization function from the training data to maximize a desired similarity metric between the reconstructed image $\hat{\mathbf{x}}$ and the ground truth. Specifically, E2E-VarNet starts with an initial estimate \mathbf{x}^0 of the solution to $\mathcal{A}\mathbf{x} = \mathbf{k}$, and uses a gradient descent scheme with respect to \mathbf{x} for a fixed number of steps T to iteratively refine its estimate and solve (2). Furthermore, it replaces the gradient of the regularization function $\Psi(\mathbf{x})$ with a neural network Φ , parametrized by θ^t at each iteration t . More formally, E2E-VarNet executes the following sequence of steps for a total of T iterations (implemented in T cascade elements similar to Fig.1), starting with $\mathbf{x}^0 = \mathcal{A}^H \mathbf{k}$:

$$\mathbf{x}^{t+1} = \mathbf{x}^t - \eta^t \mathcal{A}^H (\mathcal{A}\mathbf{x}^t - \mathbf{k}) - \Phi(\mathbf{x}^t; \theta^t), \quad (3)$$

where $\mathcal{A}^H = \mathcal{E}^H \circ \mathcal{M}$ is the Hermitian adjoint of \mathcal{A} . It is worth mentioning that the second term on the right hand side is usually referred to as *data consistency*, as it guides \mathbf{x} to be maximally consistent with the acquired measurements. At the end of iteration T , we obtain \mathbf{x}^T parameterized by $\Theta = \{\theta^0, \dots, \theta^{T-1}, \eta^0, \dots, \eta^{T-1}\}$. Assuming access to ground truth \mathbf{x}^* , parameters Θ are learned in a supervised manner to maximize a desired similarity between \mathbf{x}^T and \mathbf{x}^* .

C. Related Work

We outline how prior work has utilized side information in MR image reconstruction. While side information can take

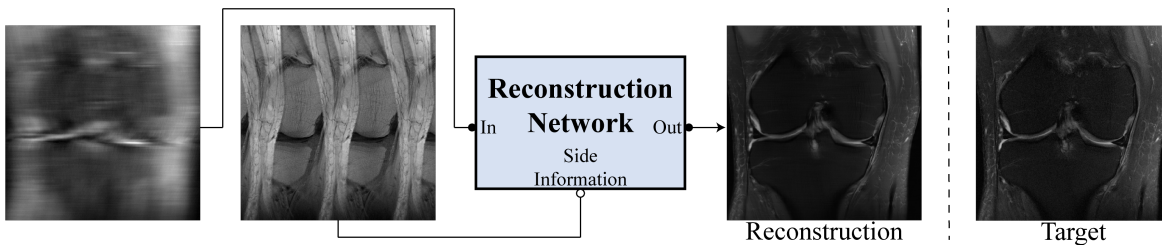


Fig. 2: Example showing the use of side information to reconstruct an image from heavily under-sampled k -space data. **Left:** Coronal PDFS image (main information) from $14\times$ under-sampled k -space data with a 3% fully-sampled center. **Middle:** Coronal PD image (side information) from $3\times$ uniformly under-sampled data. **Right:** Reconstructed coronal PDFS image along with the ground truth target image. Since PD- and PDFS-weighted scans share certain features, despite their distinct contrast and under-sampling patterns, using PD as side information to guide PDFS reconstruction is beneficial.

various forms, most studies have focused on complementary contrast information—reconstructing the target contrast by leveraging information from other contrast(s). As was mentioned earlier, this approach differs from both single-contrast and joint multi-contrast reconstruction.

Initial Attempts: The use of side information in medical image reconstruction dates back to at least the 1990s. [18] demonstrated tomographic image reconstruction based on a weighted Gibbs penalty, where the weights are determined by anatomical boundaries in high-resolution MR images. [19] proposed a Bayesian method whereby maximum a posteriori (MAP) estimates of PET and SPECT images may be reconstructed with the aid of prior information derived from registered anatomical MR images of the same slice. Some of the earlier attempts also utilized handcrafted priors [11]–[13], [20]–[27]. Later, dictionary-learning-based methods were proposed [14], [28], [29].

End-to-End Methods: More recently, multiple authors have proposed end-to-end deep learning-based models that leverage side information for MR image reconstruction. Specifically, [30], [31] proposed combining T1-weighted images and under-sampled T2-weighted images to reconstruct fully-sampled T2-weighted images using a Dense-U-net model. [15] introduced a Dilated Residual Dense Network (DuDoRNet) for dual domain restorations from under-sampled MRI data to simultaneously recover k -space and images. [32] developed a multi-modal transformer (‘MTrans’) for accelerated MR imaging which transferred multi-scale features from the target modality to the auxiliary modality. Rather than manually designing fusion rules, [16] presented a multi-contrast VarNet (‘MCVN’) to explicitly model the relationship between different contrasts.

Generative Models: Generative models utilizing side information for MR image reconstruction are GAN-based and score-based algorithms. These models can be divided into reconstruction and synthesis methods, in which the former is our focus. Specifically, [33] utilized conditional GANs with three priors—shared high-frequency, low-frequency, and perceptual priors. [34] proposed a framework for estimating objects from incomplete imaging measurements by optimizing in the latent space of a style-based generative model, using constraints from a related prior image. [35] introduced a score-based generative model (‘DMSI’) to learn a joint Bayesian prior over multi-contrast data.

Despite significant advancements, existing methods for LIPs still struggle with highly under-sampled data, often leading to degraded image quality or hallucinations. The former can be attributed to the lack of efficiency in exploiting side information, while the latter represents over-reliance on it. These limitations highlight the need for a more principled approach that can efficiently integrate additional context, maintaining consistency with acquired data while minimizing artifacts.

III. TRUST GUIDED VARIATIONAL NETWORK (TGVN)

We now give details of our proposed method, that effectively and reliably leverages *side information* to impose additional constraints into the LIP and guide the solution to fall within a contextually-appropriate distribution. In this setting, we assume that we have access to the additional side information denoted by \mathbf{s} when solving for \mathbf{x} using the system of equations $\mathcal{A}\mathbf{x} = \mathbf{k}$. So long as \mathbf{s} and \mathbf{x} are conditionally dependent given \mathbf{k} (i.e., the conditional mutual information $I(\mathbf{s}; \mathbf{x} | \mathbf{k}) > 0$), the knowledge of \mathbf{s} can be exploited to reduce the uncertainty in estimating \mathbf{x} from \mathbf{k} [36]. As such, our solution assumes the existence of such conditional dependence.

A. The Motivation: Ambiguous Space Consistency

Deep learning and physics-based unrolled networks have shown notable success in MR image reconstruction from sparse k -space data [37], [38], primarily due to their ability to enforce *data consistency*—ensuring that the reconstructed images closely match the acquired measurements. However, while data consistency is crucial for aligning the solution with the observed data, it might not be enough to resolve inherent ambiguities in the solution space, particularly at higher accelerations where an abrupt degradation in image quality has been highlighted [39], rendering the images non-diagnostic. To address this issue, we introduce the concept of *ambiguous space consistency*, which goes beyond data consistency and complements it. Essentially, our idea is to identify a subspace of images that could significantly alter reconstruction quality without substantially affecting the objective function of the MR image reconstruction problem.

Let \mathbf{x}_p be a particular solution to the equation $\mathcal{A}\mathbf{x} = \mathbf{k}$ and $U\Sigma V^H$ represent the singular value decomposition (SVD) of \mathcal{A} , where U and V are unitary matrices, and Σ is a

rectangular diagonal matrix with singular values sorted in descending order along its diagonal. Given a small positive threshold δ , we define the *ambiguous space* as the subspace spanned by the right singular vectors (columns of V) with corresponding singular values smaller than δ and denote it as $\mathcal{W}_\delta(\mathcal{A})$. Observe that if we add any unit vector $\mathbf{x}_a \in \mathcal{W}_\delta(\mathcal{A})$ to \mathbf{x}_p , the data consistency distance $\|\mathcal{A}(\mathbf{x}_p + \mathbf{x}_a) - \mathbf{k}\|_2^2$ can at most be δ^2 . In other words, perturbing a solution that aligns with the observed measurements by adding a vector from the ambiguous space results in only a minor change to the objective value. However, only certain \mathbf{x}_a maximize the desired similarity between $\mathbf{x}_p + \mathbf{x}_a$ and \mathbf{x}^* , indicating that, once a particular solution is found, images from $\mathcal{W}_\delta(\mathcal{A})$ introduce ambiguity in the reconstruction problem. That is, they might visually alter the reconstruction quality without significantly affecting the loss. Inspired by this observation, we propose to explicitly learn a constraint that removes undesirable solutions from $\mathcal{W}_\delta(\mathcal{A})$. Our idea is to project \mathbf{x} onto $\mathcal{W}_\delta(\mathcal{A})$ with the orthogonal projector \mathcal{P}_δ and to guide \mathbf{x} to be maximally consistent with the side information \mathbf{s} using a learnable module \mathcal{H} parametrized by γ . Specifically, we add a squared Euclidean distance constraint $\|\mathcal{P}_\delta \mathbf{x} - \mathcal{H}(\mathbf{s}; \gamma)\|_2^2$ to (2) to obtain

$$\hat{\mathbf{x}} = \arg \min_{\mathbf{x}} \frac{1}{2} \|\mathcal{A} \mathbf{x} - \mathbf{k}\|_2^2 + \frac{\beta}{2} \|\mathcal{P}_\delta \mathbf{x} - \mathcal{H}(\mathbf{s}; \gamma)\|_2^2 + \Psi(\mathbf{x}). \quad (4)$$

Our reason for choosing a more general projector \mathcal{P}_δ rather than simply using an orthogonal projector onto the null space of \mathcal{A} is twofold. First, in practice, the forward operator matrix \mathcal{A} in parallel MR imaging and other LIPs can have a trivial null space but still exhibit many small, non-zero singular values. This is the reason for high noise amplification at higher acceleration rates [40]. Second, even when the null space is non-trivial (i.e., it does not only contain the zero vector), the presence of small singular values can pose challenges, and the proposed approach can further assist in resolving these ambiguities.

B. The Solution: Iterative Optimization

The solution to (4) can be obtained using a cascade of neural networks similar to those used in the E2E-VarNet method. As the added constraint involves only a squared Euclidean distance, its integration into (3) is straightforward. Starting with $\mathbf{x}_0 = \mathcal{A}^H \mathbf{k}$, we execute the following sequence of steps for a total of T iterations.

$$\mathbf{x}^{t+1} = \mathbf{x}^t - \eta^t \mathcal{A}^H (\mathcal{A} \mathbf{x}^t - \mathbf{k}) - \underbrace{\mu^t \mathcal{P}_\delta (\mathbf{x}^t - \mathcal{H}(\mathbf{s}; \gamma^t))}_{\text{trust-guidance}} - \Phi(\mathbf{x}^t; \theta^t). \quad (5)$$

At the end of the iteration T , we obtain \mathbf{x}^T parameterized by $\Omega \triangleq \Theta \cup \{\delta, \gamma^0, \dots, \gamma^{T-1}, \mu^0, \dots, \mu^{T-1}\}$. Assuming access to ground truth \mathbf{x}^* , the parameters Ω are learned in a supervised manner to maximize a desired similarity between \mathbf{x}^T and \mathbf{x}^* . It is worth noting that the parameter δ can be learned from the data as proposed, or it can be fixed based on

the coil specifications and under-sampling pattern by analyzing the distribution of singular values.

In high-dimensional problems like parallel MR imaging, the computational burden of working directly with large-scale operators can be prohibitive. Therefore, instead of explicitly calculating the SVD of the forward operator, which would be computationally expensive, we seek an efficient alternative. Here, we present an efficient approximation of the exact orthogonal projector \mathcal{P}_δ , which bypasses the need for SVD computation. This approach is crucial for managing the scale of the forward operator, which may contain hundreds of thousands of rows and columns, making explicit methods infeasible. For a set \mathcal{K} , Let $1_{\mathcal{K}}(x)$ denote an indicator function that equals 1 if $x \in \mathcal{K}$ and 0 otherwise. Given δ , the exact projector can be written as $\mathcal{P}_\delta = \sum_i 1_{[0, \delta)}(\sigma_i) \mathbf{v}_i \mathbf{v}_i^H$. Instead of assigning binary weights to the i th projection, we can weight them by $\delta^2 / (\delta^2 + \sigma_i^2)$, and define

$$\mathcal{P}'_\delta \triangleq \sum_i \frac{\delta^2}{\delta^2 + \sigma_i^2} \mathbf{v}_i \mathbf{v}_i^H = \left(I + \frac{1}{\delta^2} \mathcal{A}^H \mathcal{A} \right)^{-1}, \quad (6)$$

where $I : \mathbf{x} \mapsto \mathbf{x}$ denotes the identity operator.

IV. EMPIRICAL VALIDATION

We validated the efficacy of TGVN by using it for multi-coil MR image reconstruction from different contrasts across different anatomies and field strengths. In all experiments, we utilized the efficient approximate projection introduced in (6). In our empirical validation, we sought answers to the following four questions:

- Q1) Is there any benefit in using the side information?
- Q2) How effective is TGVN at utilizing the side information?
- Q3) Does projecting onto the *ambiguous space* provide any benefits compared to no projection?
- Q4) How robust is the proposed approach to different under-sampling factors, to misregistration between images used for main and side information, and to degradation in the quality of side information?

To answer Q1, we compared the reconstruction performance of our TGVN against an E2E-VarNet of the same capacity that does not utilize side information. Q2 was answered by comparing the performance of TGVN against several recent deep-learning baselines that also leverage side information in image reconstruction: MTrans [32], MCVN [16], and DMSI [35]. To address Q3, we compared the performance of TGVN with and without the projection. Q4 was answered by conducting experiments using multiple under-sampling factors and deliberately introduced misregistrations. We present our findings related to the first and second questions in Section V-A and V-B. Our findings related to the third and fourth questions are presented in the Appendix and Supplementary Material, which show that projection onto the ambiguous space significantly improves TGVN's performance and that TGVN is robust to moderate under-sampling and misregistration of side information.

In our experiments, under-sampling was implemented along the phase-encoding direction. The target images were selected as the root-sum-of-squares (RSS) combination $\sqrt{\sum_i |\mathbf{x}_i|^2}$ of

TABLE I: Quantitative evaluation results: SSIM, PSNR, and NRMSE are shown for the knee (I, II) and brain (III) experiments using TGVN and various baseline methods. For each evaluation metric and each reconstruction method, the mean and standard error of the mean over the test dataset are reported. Bold-face values indicate the best performance in each category, which in all cases is achieved by TGVN reconstruction. For SSIM and PSNR, higher is better; for NRMSE, lower is better.

Metric	Experiment	TGVN	DMSI	MCVN	MTrans	E2E-VarNet
SSIM	I	84.92 ± 0.19	56.99 ± 0.31	82.89 ± 0.21	80.84 ± 0.23	81.33 ± 0.23
	II	85.52 ± 0.19	58.76 ± 0.31	83.13 ± 0.21	81.25 ± 0.22	83.40 ± 0.21
	III	87.34 ± 0.12	–	86.95 ± 0.12	84.03 ± 0.14	75.63 ± 0.18
PSNR	I	30.92 ± 0.07	22.22 ± 0.10	29.97 ± 0.07	28.93 ± 0.07	29.30 ± 0.07
	II	31.31 ± 0.07	22.68 ± 0.10	30.07 ± 0.07	29.11 ± 0.07	30.37 ± 0.07
	III	30.81 ± 0.08	–	30.75 ± 0.08	28.70 ± 0.08	24.60 ± 0.09
NRMSE	I	0.14 ± 0.001	0.40 ± 0.004	0.16 ± 0.001	0.18 ± 0.001	0.17 ± 0.001
	II	0.13 ± 0.001	0.38 ± 0.004	0.16 ± 0.001	0.17 ± 0.001	0.15 ± 0.001
	III	0.158 ± 0.002	–	0.159 ± 0.002	0.201 ± 0.002	0.32 ± 0.004

fully-sampled component coil images \mathbf{x}_i . We evaluated the reconstruction quality using three metrics: the structural similarity index [41] (SSIM), peak signal-to-noise ratio (PSNR), and normalized root-mean-squared error (NRMSE). For the SSIM metric, a 7×7 uniform kernel was utilized, along with the standard k -values of 0.01 and 0.03. The range parameter is given as input to the SSIM calculation and is set to the maximum pixel value of the corresponding volume. To demonstrate the statistical significance of the improvements in image reconstruction metrics, we performed a Wilcoxon signed-rank test [42] between the metrics calculated on the test dataset for TGVN (s_{ours}) as compared with the best-performing baseline (s_{base} , the baseline with the best average score). Let \mathcal{D} be the distribution of pairwise difference $s_{\text{ours}} - s_{\text{base}}$. Then under the alternate hypothesis, \mathcal{D} is “stochastically greater than a distribution symmetric about zero” for SSIM and PSNR and “stochastically less than a distribution symmetric about zero” for NRMSE. Additional training and evaluation details are presented in the Supplementary Material.

In knee experiments, we utilized a subset of the multi-coil track of the fastMRI knee dataset—an open-source dataset consisting of k -space measurements from clinical 3T and 1.5T scanners paired with ground truth clinical cross-sectional images [43]. Our dataset comprised coronal MR scans of 428 patients using a proton-density weighting with fat suppression (PDFS) and proton density weighting without fat suppression (PD). Data acquisition employed a 15-channel knee coil array and Cartesian 2D Turbo Spin Echo (TSE) pulse sequences. The dataset consisted of 368, 30, and 30 image volumes for training, validation, and test sets, respectively, with a total of 15, 231 slices.

Brain experiments utilized the M4Raw dataset [44]—a publicly available multi-channel k -space dataset of brain scans of 183 healthy volunteers acquired using a low-field (0.3T) scanner. It includes axial MR scans with three contrasts, acquired using a 4-channel array: T1-weighted (T1w), T2-weighted (T2w), and fluid-attenuated inversion recovery (FLAIR). Each scan has 18 slices per contrast with varying numbers of repetitions. We used single-repetition measurements to reconstruct images with quality similar to that of multi-repetition aggregated RSS targets. The training, validation, and test sets

included 128, 30, and 25 volumes, respectively.

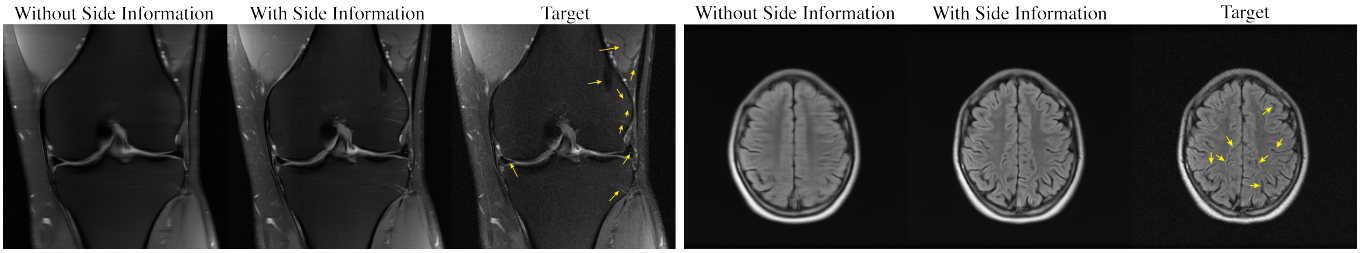
V. RESULTS

A. Knee Experiments

In our experiments involving knee MR images, we treated the highly under-sampled PDFS-weighted k -space measurements as the “main information” and reconstructed a PDFS-weighted RSS image from them, using the corresponding moderately under-sampled PD k -space measurements (which we treated as “side information”). To evaluate TGVN’s effectiveness in diverse settings, we conducted two experiments with different sampling rates in main and side information, encompassing both the non-trivial and the trivial null space cases (i.e., acceleration factors greater than and less than the number of coils), respectively. Additional details are provided in the Supplementary Material.

Set I – $20\times$ Under-sampled Main Information and $2\times$ Under-sampled Side Information: We applied an overall $20\times$ undersampling mask to the PDFS measurements, with random outer undersampling and a 3% fully-sampled center. A $2\times$ equispaced under-sampling mask with no fully-sampled center was applied to the PD measurements. Fig. 3a shows the reconstruction results for coronal PDFS images with and without using the side information. At $20\times$ acceleration, side information aids the reconstruction significantly while reconstruction without side information results in the loss of various essential features. Fig. 4 compares TGVN reconstructions with reconstructions using multiple baselines that use side information. MTrans and MCVN exhibit significant blurring of anatomical features, and DMSI suffers severely from noise amplification, which is seen clearly in the absolute difference images. The output of TGVN is significantly superior: both overall sharpness and assorted anatomical details are better preserved in the TGVN reconstructions. Furthermore, the meniscus tear region is distinctly more noticeable with TGVN, highlighting that it is *more effective* in leveraging the side information to preserve key features in the image despite highly sparse measurements.

Set II – $14\times$ Under-sampled Main Information and $3\times$ Under-sampled Side Information: We applied an overall



(a) Coronal PDFS knee image reconstruction without and with side information at $20\times$ acceleration (b) Axial FLAIR brain image reconstruction without and with side information at $36\times$ acceleration.

Fig. 3: Leveraging side information significantly enhances the reconstruction quality. Left: Reconstructed MR image from highly sparse MR measurements using E2E-VarNet. **Middle:** Reconstructed MR image from the same sparse MR measurements, with additional side information from a different sequence using TGVN (having the same capacity as the E2E-VarNet). **Right:** Ground truth target image, with prominent anatomical features highlighted by yellow arrows.

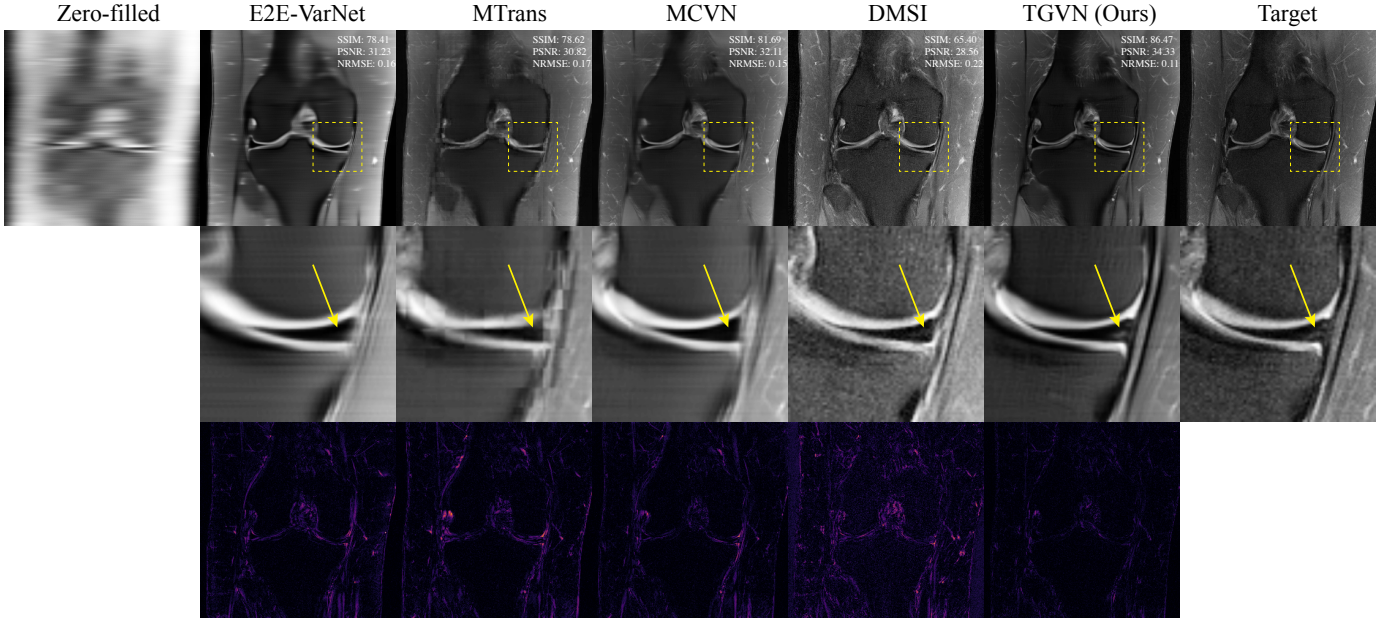


Fig. 4: Knee image reconstructions from Set I showing the effectiveness of TGVN in leveraging side information. TGVN is able to reconstruct a high-quality image even at challenging acceleration levels of $20\times$, in comparison to various baselines. The *meniscus tear*, illustrated in the ground truth image and reconstructions with a yellow arrow, is notably more visible in the TGVN reconstruction than in baseline reconstructions. **Top:** Full field of view images. **Middle:** Zoomed-in regions indicated by dashed yellow boxes in the top row. **Bottom:** Absolute differences between each reconstruction and the ground truth, with a consistent color mapping to highlight error magnitudes. TGVN has the smallest error.

$14\times$ under-sampling mask to the PDFS measurements, with random outer undersampling and a 3% fully-sampled center. Additionally, a $3\times$ equispaced under-sampling mask with no fully-sampled center was applied to the PD measurements. It is worth noting that knee images are acquired with 15 coils, which implies that, in this experiment, the null space is trivial, i.e., it contains only the zero vector. Therefore, methods utilizing the range-null space decomposition are unlikely to be effective. Fig. 2 illustrates example input, side information, and target images for this experiment.

Table I reports the quantitative evaluation of TGVN as compared with baselines in both sets of experiments. TGVN achieves the best average score across all metrics, proving that it is more effective than any of the baselines in utilizing side information. In each experiment and for each evaluation

metric (SSIM, PSNR, and NRMSE), a Wilcoxon signed-rank test rejected the null hypothesis at a significance level of 5%, indicating that there is a statistically significant difference between s_{ours} and s_{base} . We provide additional details regarding reconstructions and evaluation results in the Supplementary Material, showing that TGVN has superior performance for *almost all examples* in the test dataset for each experiment.

B. Brain Experiments

In our experiments using brain MR images, we used highly under-sampled FLAIR k -space measurements from a single repetition as the “main information,” aiming to generate reconstructions with image quality approaching that of signal-averaged multi-repetition FLAIR RSS images. As

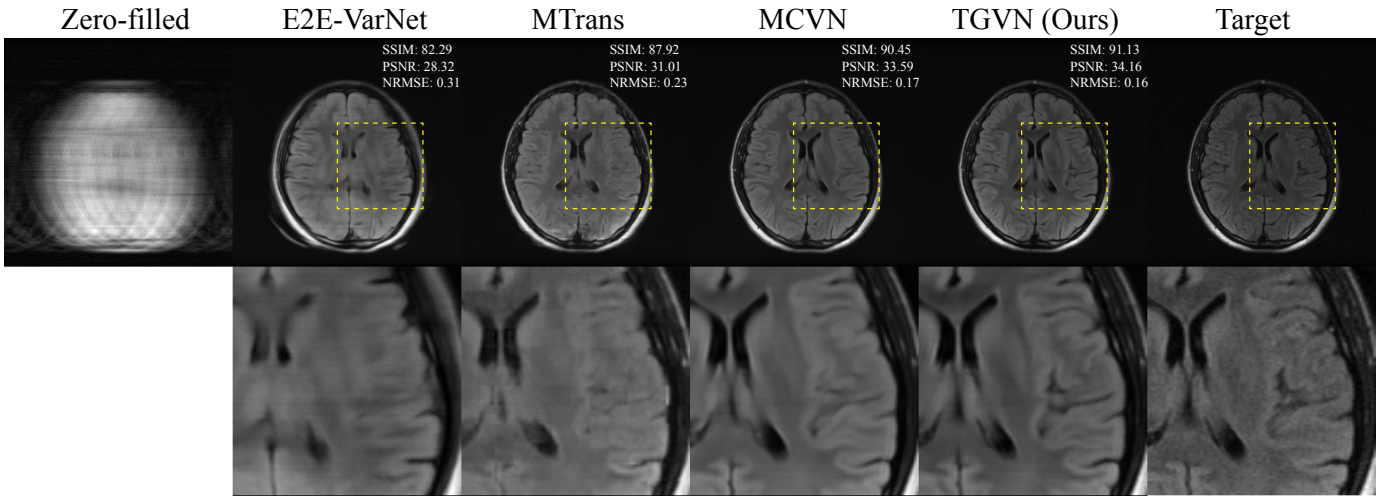


Fig. 5: Brain image reconstructions from Set III showing the effectiveness of TGVN at the challenging acceleration level of $36\times$ ($18\times$ undersampling and $2\times$ repetition reduction), in comparison to baselines (DMSI omitted since it does not handle repetition reduction). **Top: Full field of view images. **Bottom:** Zoomed-in regions indicated by dashed yellow boxes in the top row, windowed up for better visualization. TGVN preserves structural details which are obscured by other methods.**

“side information” we used corresponding low-SNR, single-repetition T2-weighted (T2w) k -space measurements. We selected FLAIR as the main information and T2w as the side information because, in the protocol described by [44], FLAIR has the longest acquisition time per repetition (135 seconds), while T2w has the shortest (71.5 seconds). Note that the protocol includes two repetitions for FLAIR and three for T2w. Hence, by using a single repetition as side information, we achieve a practical acceleration factor of $3\times$.

Set III – $18\times$ Under-sampled Main Information and Single-repetition Side Information: We applied an overall $18\times$ under-sampling mask to the FLAIR measurements from a single repetition, with $32\times$ equispaced outer undersampling and a 2% fully-sampled center. Between $18\times$ k -space undersampling and $2\times$ repetition reduction we achieved a practical acceleration factor of $36\times$. We chose the equispaced mask in these experiments to evaluate the proposed method in a setting complementary to the random undersampling used in the knee experiments. Fully-sampled T2w images were used as side information, in light of the low SNR and small matrix size of the acquisition [44]. Fig. 3b shows the reconstruction results for axial FLAIR images with and without using the side information. At $36\times$ practical acceleration, side information aids the reconstruction significantly while reconstruction without side information results in the loss of various essential features. Fig. 5 juxtaposes axial FLAIR images reconstructed using TGVN with corresponding images reconstructed using baseline methods. Use of side information results in substantial improvements in image quality at the challenging practical acceleration level of $36\times$. TGVN demonstrates superior performance in integrating this information compared to other methods, as evidenced by the enhanced depiction of anatomical features in the zoomed-in region and the consistently improved reconstruction metrics. Furthermore, for each quantitative evaluation metric (SSIM, PSNR, and NRMSE), a Wilcoxon signed-rank test rejected the null hy-

pothesis at a significance level of 5%, indicating that there is a statistically significant difference between s_{ours} and s_{base} . Table I reports the quantitative evaluation results for TGVN as compared with baselines. As is the case for knee experiments, TGVN again achieves the best average score across all metrics. The statistically significant performance difference between TGVN and baseline methods indicates the side information is beneficial in guiding the reconstruction, and that TGVN is more effective than other methods at leveraging it. Additional evaluation results are provided in the Supplementary Material, demonstrating further statistically significant improvements.

VI. CONCLUSION

Our work introduces a novel framework, the Trust-Guided Variational Network (TGVN), that demonstrates the power of leveraging side information in solving LIPs, with specific application to the MR image reconstruction problem. By learning to eliminate solutions from the *ambiguous space* of the forward operator while remaining faithful to acquired measurements through *data consistency*, our principled approach makes maximal use of relevant side information while minimizing the risk of hallucinations. Our key finding is that, when incorporated effectively, side information can significantly improve reconstruction quality and preserve key anatomical and pathological features, even at very high levels of under-sampling or other means of acceleration. High levels of acceleration, meanwhile, can have a transformative impact in healthcare, by improving imaging efficiency in traditional settings, and also by enabling use of lower-quality data from accessible imaging devices for widespread health monitoring at the population level.

While the results for MR image reconstruction using TGVN are already very promising, as of yet we have only used complementary-contrast measurements from the same MR examination as side information. In the future, we intend to explore incorporation of different types of side information,

including a patient’s prior scans and associated textual data (e.g., clinical notes and medical history), as well as features learned from related tasks.

APPENDIX

We conducted ablation studies to answer Q3 and Q4, which were introduced in Sec. IV. To answer Q3, we compared our proposed method with and without the projection (Sec. A). In particular, we compared the reconstruction performance of the unrolled network implementing (5) and the unrolled network implementing a modified version of (5) in which \mathcal{P}_δ is replaced by the identity operator. Starting with $\mathbf{x}_0 = \mathcal{A}^H \mathbf{k}$, the network without the projection implements the following update equations for T iterations:

$$\begin{aligned} \mathbf{x}^{t+1} = & \mathbf{x}^t - \eta^t \mathcal{A}^H (\mathcal{A} \mathbf{x}^t - \mathbf{k}) \\ & - \mu^t (\mathbf{x}^t - \mathcal{H}(\mathbf{s}; \gamma^t)) - \Phi(\mathbf{x}^t; \theta^t). \end{aligned} \quad (7)$$

Q4 was answered by conducting two experiments. In the misregistration ablation study (Sec. B.1), we compared the performance of TGVN when the side information is perfectly registered with performance in the presence of random misregistrations simulated by small random shifts and rotations during training and/or inference. In the under-sampling ablation study (Sec. B.2), we compared the performance of three models: (I) TGVN utilizing under-sampled side information; (II) TGVN utilizing under-sampled side information reconstructed first with an E2E-VarNet; and (III) TGVN utilizing fully-sampled side information. We note that the TGVNs in (I), (II), and (III) have the same number of parameters; however, inclusion of the additional high-capacity E2E-VarNet in (II) introduces a minor element of unfairness in the comparison.

A. Effect of Projection

We applied an overall $9\times$ under-sampling mask with equispaced $15\times$ outer undersampling and a 4% fully-sampled center to the FLAIR measurements from a single repetition, achieving a practical acceleration factor of $18\times$. As in experiment III, fully-sampled T2w images were used as side information. We performed three Wilcoxon signed-rank tests, and they rejected the null hypotheses at a significance level of 5%, concluding that there is a statistically significant difference between $s_{w/}$ and $s_{w/o}$, where $s_{w/}$ and $s_{w/o}$ represent the SSIM, PSNR, and NRMSE scores calculated on the test dataset for the TGVN with and without the proposed projector, respectively. Suppl. Fig. 1 presents quantitative evaluation results for the effect of projection, demonstrating that the projection improves reconstruction quality for almost all slices in the test dataset.

B. Robustness to Degraded Side Information

1) *Misregistration*: For this experiment, we applied the same $9\times$ undersampling / $18\times$ acceleration scheme as in Sec. A. For each slice, three random variables, dx , dy , and $d\theta$, were drawn uniformly from the interval $[-4, 4]$, and side information was translated by dx and dy pixels and rotated by $d\theta$ degrees. As expected, we observed that if TGVN does not encounter misregistration during training, the substantially during inference.

TABLE II: Quantitative evaluation results (SSIM, PSNR, and NRMSE) for the Ablation Study B.2. Bold-face values indicate the best performance in each category.

Metric/Model	$3\times$ under-sampled s	$3\times$ under-sampled s, two-stage	Fully-sampled s
SSIM	85.52 \pm 0.19	85.56 \pm 0.19	85.97 \pm 0.18
PSNR	31.31 \pm 0.07	31.41 \pm 0.07	31.60 \pm 0.07
NRMSE	0.13 \pm 0.001	0.13 \pm 0.001	0.13 \pm 0.001

However, data augmentation with small random misregistrations during training render the TGVN robust to small misregistrations during inference, as seen in Suppl. Fig. 2. With such augmentation, TGVN still achieves significantly better scores than E2E-VarNet of the same capacity. This observation is supported by Wilcoxon tests at a 5% significance level for each metric—SSIM, PSNR, and NRMSE—demonstrating a statistically significant performance differences in favor of TGVN with misregistered side information, as compared to E2E-VarNet, which does not utilize side information. This observation is also supported by Suppl. Fig. 3.

2) *Under-sampling*: We applied an overall $14\times$ random outer under-sampling mask with a 3% fully-sampled center to the PDFS measurements. Additionally, a $3\times$ equispaced under-sampling mask with no fully-sampled center was applied to the PD measurements as side information for one TGVN (I), while fully-sampled PD side information was provided to another TGVN (III). For a third TGVN (II), a two-stage reconstruction was used, in which the $3\times$ under-sampled side information was first reconstructed with an E2E-VarNet with 30 million trainable parameters, and the reconstructed result was then utilized as side information for the TGVN. We observed that the reconstruction scores improve with fully-sampled side information, but the improvements are slight and difficult to appreciate visually. Furthermore, despite having 30 million more trainable parameters to work with, the two-stage approach did not provide statistically significant improvements compared to TGVN utilizing under-sampled side information. Quantitative evaluation results for this experiment are provided in Table II, and an example reconstruction from this study is shown in Suppl. Fig. 4. Our takeaway from this experiment is that while fully-sampled side information provides the greatest benefit, moderately under-sampled side information is still helpful, significantly improving the reconstruction compared to not having any side information (cf. Table I, E2E-VarNet column). Furthermore, end-to-end training with under-sampled side information performs as well as the two-stage approach (first reconstructing the under-sampled side information, then using the reconstructed side information with the TGVN).

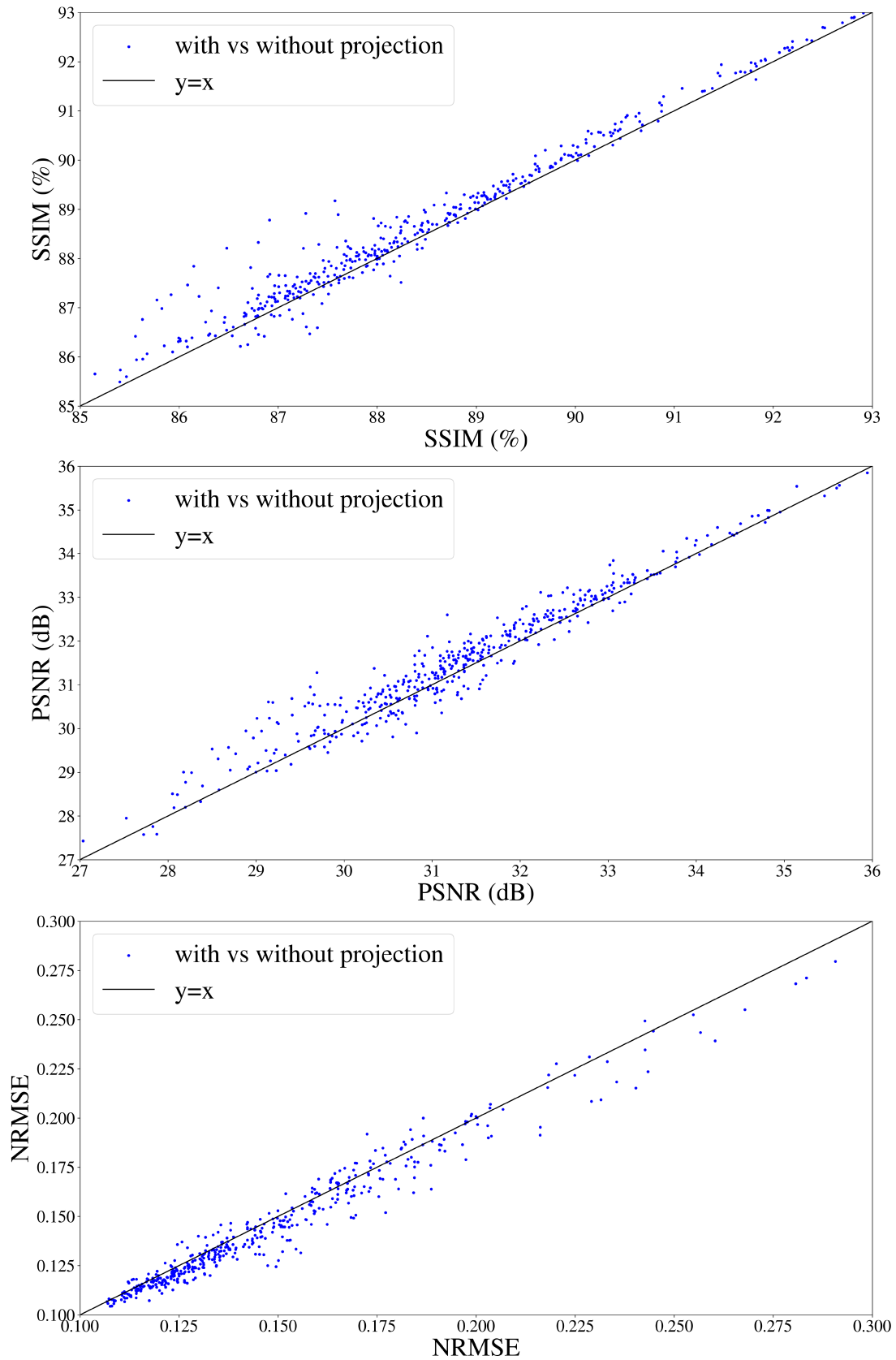
C. Detailed Evaluation Results and Further Reconstruction Examples

Suppl. Fig. 5, Suppl. Fig. 6, and Suppl. Fig. 7 present quantitative evaluation results on the test split for TGVN and the second-best method for each of Experiment I, II, and III, respectively, as scatter plots, demonstrating the consistent improvements provided by TGVN over baselines. Suppl. Fig. 8

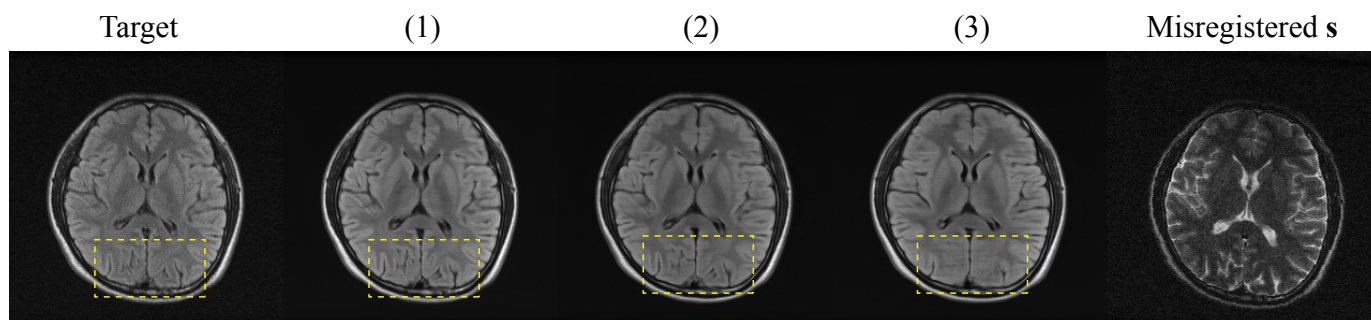
shows a knee image reconstruction not included in the main text, and the same reconstruction is shown in Suppl. Fig. 9 with noise added to match the subjective noise level of the target, for enhanced visual comparison and to demonstrate preservation of features despite the the TGVN's inherent denoising properties.

REFERENCES

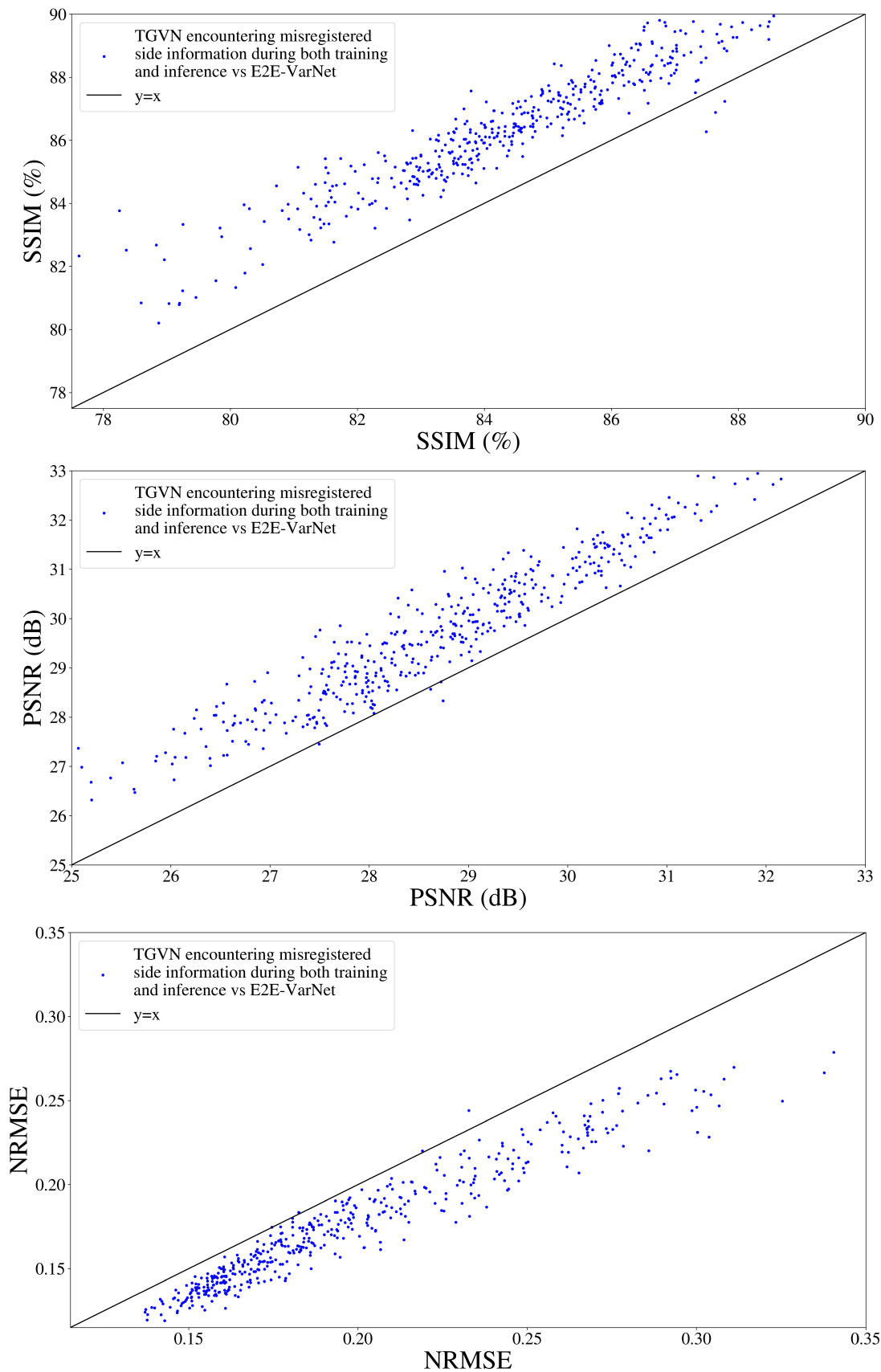
- [1] M. Lustig, D. L. Donoho, and J. M. Pauly, "Sparse MRI: The application of compressed sensing for rapid MR imaging," *Magn. Reson. Med.*, vol. 58, no. 6, pp. 1182–1195, 2007.
- [2] S. Ravishanker and Y. Bresler, "MR image reconstruction from highly undersampled k-space data by dictionary learning," *IEEE Trans. Med. Imaging*, vol. 30, no. 5, pp. 1028–1041, 2010.
- [3] J. Caballero, A. N. Price, D. Rueckert, and J. V. Hajnal, "Dictionary learning and time sparsity for dynamic MR data reconstruction," *IEEE Trans. Med. Imaging*, vol. 33, no. 4, pp. 979–994, 2014.
- [4] K. Hammernik, T. Klatzer, E. Kobler, M. P. Recht, D. K. Sodickson, T. Pock, and F. Knoll, "Learning a variational network for reconstruction of accelerated MRI data," *Magn. Reson. Med.*, vol. 79, no. 6, pp. 3055–3071, 2018.
- [5] A. Sriram, J. Zbontar, T. Murrell, A. Defazio, C. L. Zitnick, N. Yakubova, E. Owens, D. K. Sodickson, F. Knoll, and P. Johnson, "End-to-end variational networks for accelerated MRI reconstruction," *Med. Image Anal.*, vol. 73, pp. 34–47, 2021.
- [6] H. K. Aggarwal, M. P. Mani, and M. Jacob, "MoDL: Model-Based Deep Learning Architecture for Inverse Problems," *IEEE Trans. Med. Imaging*, vol. 38, no. 2, pp. 394–405, 2019.
- [7] J. Xiang, Y. Dong, and Y. Yang, "FISTA-Net: Learning a fast iterative shrinkage thresholding network for inverse problems in imaging," *IEEE Trans. Med. Imaging*, vol. 40, no. 5, pp. 1329–1339, 2021.
- [8] A. Bora, A. Jalal, E. Price, and A. G. Dimakis, "Compressed sensing using generative models," in *Proc. Int. Conf. Mach. Learn.*, 2017, pp. 537–546.
- [9] H. Chung and J. C. Ye, "Score-based diffusion models for accelerated MRI," *Med. Image Anal.*, vol. 80, p. 102479, 2022.
- [10] Y. Song, L. Shen, L. Xing, and S. Ermon, "Solving Inverse Problems in Medical Imaging with Score-Based Generative Models," in *Proc. Int. Conf. Learn. Represent.*, 2022.
- [11] L. Weizman, Y. C. Eldar, and D. Ben Bashat, "Compressed sensing for longitudinal MRI: an adaptive-weighted approach," *Med. Phys.*, vol. 42, no. 9, pp. 5195–5208, 2015.
- [12] —, "Reference-based MRI," *Med. Phys.*, vol. 43, no. 10, pp. 5357–5369, 2016.
- [13] M. J. Ehrhardt and M. M. Betcke, "Multicontrast MRI reconstruction with structure-guided total variation," *SIAM J. Imaging Sci.*, vol. 9, no. 3, pp. 1084–1106, 2016.
- [14] P. Song, L. Weizman, J. F. Mota, Y. C. Eldar, and M. R. Rodrigues, "Coupled dictionary learning for multi-contrast MRI reconstruction," *IEEE Trans. Med. Imaging*, vol. 39, no. 3, pp. 621–633, 2019.
- [15] B. Zhou and S. K. Zhou, "DuDoRNet: learning a dual-domain recurrent network for fast MRI reconstruction with deep T1 prior," in *Proc. IEEE/CVF Conf. Comput. Vis. Pattern Recognit.*, 2020, pp. 4273–4282.
- [16] P. Lei, F. Fang, G. Zhang, and T. Zeng, "Decomposition-based variational network for multi-contrast MRI super-resolution and reconstruction," in *Proc. IEEE/CVF Int. Conf. Comput. Vis.*, 2023, pp. 21 296–21 306.
- [17] P. C. Hansen, *Discrete Inverse Problems: Insight and Algorithms*. SIAM, 2010.
- [18] J. A. Fessler, N. H. Clinthorne, and W. L. Rogers, "Regularized emission image reconstruction using imperfect side information," *IEEE Trans. Nucl. Sci.*, vol. 39, no. 5, pp. 1464–1471, 1992.
- [19] G. Gindi, M. Lee, A. Rangarajan, and I. G. Zubal, "Bayesian reconstruction of functional images using anatomical information as priors," *IEEE Trans. Med. Imaging*, vol. 12, no. 4, pp. 670–680, 1993.
- [20] J. P. Haldar, D. Hernando, S.-K. Song, and Z.-P. Liang, "Anatomically constrained reconstruction from noisy data," *Magn. Reson. Med.*, vol. 59, no. 4, pp. 810–818, 2008.
- [21] B. Wu, R. P. Millane, R. Watts, and P. J. Bones, "Prior estimate-based compressed sensing in parallel MRI," *Magn. Reson. Med.*, vol. 65, no. 1, pp. 83–95, 2011.
- [22] X. Peng, H.-Q. Du, F. Lam, S. D. Babacan, and Z.-P. Liang, "Reference-driven MR image reconstruction with sparsity and support constraints," in *Proc. IEEE Int. Symp. Biomed. Imaging*. IEEE, 2011, pp. 89–92.
- [23] B. Bilgic, V. K. Goyal, and E. Adalsteinsson, "Multi-contrast reconstruction with Bayesian compressed sensing," *Magn. Reson. Med.*, vol. 66, no. 6, pp. 1601–1615, 2011.
- [24] H. Du and F. Lam, "Compressed sensing MR image reconstruction using a motion-compensated reference," *Magn. Reson. Imaging*, vol. 30, no. 7, pp. 954–963, 2012.
- [25] J. Huang, C. Chen, and L. Axel, "Fast multi-contrast MRI reconstruction," *Magn. Reson. Imaging*, vol. 32, no. 10, pp. 1344–1352, 2014.
- [26] X. Qu, Y. Hou, F. Lam, D. Guo, J. Zhong, and Z. Chen, "Magnetic resonance image reconstruction from undersampled measurements using a patch-based nonlocal operator," *Med. Image Anal.*, vol. 18, no. 6, pp. 843–856, 2014.
- [27] G. Li, J. Hennig, E. Raitchel, M. Büchert, D. Paul, J. G. Korvink, and M. Zaitsev, "Incorporation of image data from a previous examination in 3D serial MR imaging," *Magn. Reson. Mater. Phys. Biol. Med.*, vol. 28, pp. 413–425, 2015.
- [28] A. Gungor, E. Kopanoglu, T. Cukur, E. Guven, and F. T. Yarman-Vural, "Joint dictionary learning reconstruction of compressed multi-contrast Magnetic Resonance Imaging," in *Natl. Biomed. Eng. Meet. IEEE*, 2017, pp. i–iv.
- [29] P. Lei, F. Fang, G. Zhang, and M. Xu, "Deep unfolding convolutional dictionary model for multi-contrast MRI super-resolution and reconstruction," in *Proc. Int. Joint Conf. Artif. Intell.*, 2023, pp. 1008–1016.
- [30] L. Xiang, Y. Chen, W. Chang, Y. Zhan, W. Lin, Q. Wang, and D. Shen, "Ultra-fast T2-weighted MR reconstruction using complementary T1-weighted information," in *Proc. Int. Conf. Med. Image Comput. Comput.-Assist. Intervent.* Springer, 2018, pp. 215–223.
- [31] —, "Deep-learning-based multi-modal fusion for fast MR reconstruction," *IEEE Trans. Biomed. Eng.*, vol. 66, no. 7, pp. 2105–2114, 2019.
- [32] C.-M. Feng, Y. Yan, G. Chen, Y. Xu, Y. Hu, L. Shao, and H. Fu, "Multimodal transformer for accelerated MR imaging," *IEEE Trans. Med. Imaging*, vol. 42, no. 10, pp. 2804–2816, 2022.
- [33] S. U. Dar, M. Yurt, M. Shahdloo, M. E. Ildiz, B. Tinaz, and T. Çukur, "Prior-guided image reconstruction for accelerated multi-contrast MRI via generative adversarial networks," *IEEE J. Sel. Top. Signal Process.*, vol. 14, no. 6, pp. 1072–1087, 2020.
- [34] V. A. Kelkar and M. Anastasio, "Prior Image-Constrained Reconstruction using Style-Based Generative Models," in *Proc. Int. Conf. Mach. Learn.*, vol. 139, 2021, pp. 5367–5377.
- [35] B. Levac, A. Jalal, K. Ramchandran, and J. I. Tamir, "MRI reconstruction with side information using diffusion models," in *Proc. Asilomar Conf. Signals, Syst., Comput.* IEEE, 2023, pp. 1436–1442.
- [36] T. M. Cover and J. A. Thomas, *Elements of Information Theory*, 2nd ed. Wiley-Interscience, 2006.
- [37] F. Knoll, T. Murrell, A. Sriram, N. Yakubova, J. Zbontar, M. Rabbat, A. Defazio, M. J. Muckley, D. K. Sodickson, C. L. Zitnick *et al.*, "Advancing machine learning for MR image reconstruction with an open competition: Overview of the 2019 fastMRI challenge," *Magn. Reson. Med.*, vol. 84, no. 6, pp. 3054–3070, 2020.
- [38] M. J. Muckley, B. Riemenschneider, A. Radmanesh, S. Kim, G. Jeong, J. Ko, Y. Jun, H. Shin, D. Hwang, M. Mostapha *et al.*, "Results of the 2020 fastMRI challenge for machine learning MR image reconstruction," *IEEE Trans. Med. Imaging*, vol. 40, no. 9, pp. 2306–2317, 2021.
- [39] A. Radmanesh, M. J. Muckley, T. Murrell, E. Lindsey, A. Sriram, F. Knoll, D. K. Sodickson, and Y. W. Lui, "Exploring the acceleration limits of deep learning variational network-based two-dimensional brain MRI," *Radiol. Artif. Intell.*, vol. 4, no. 6, p. e210313, 2022.
- [40] K. P. Pruessmann, M. Weiger, M. B. Scheidegger, and P. Boesiger, "SENSE: sensitivity encoding for fast MRI," *Magn. Reson. Med.*, vol. 42, no. 5, pp. 952–962, 1999.
- [41] Z. Wang, A. C. Bovik, H. R. Sheikh, and E. P. Simoncelli, "Image quality assessment: from error visibility to structural similarity," *IEEE Trans. Image Process.*, vol. 13, no. 4, pp. 600–612, 2004.
- [42] F. Wilcoxon, "Individual comparisons by ranking methods," *Biometrics*, vol. 1, no. 6, pp. 80–83, 1945.
- [43] F. Knoll, J. Zbontar, A. Sriram, M. J. Muckley, M. Bruno, A. Defazio, M. Parente, K. J. Geras, J. Katsnelson, H. Chandarana *et al.*, "fastMRI: A publicly available raw k-space and DICOM dataset of knee images for accelerated MR image reconstruction using machine learning," *Radiol. Artif. Intell.*, vol. 2, no. 1, p. e190007, 2020.
- [44] M. Lyu, L. Mei, S. Huang, S. Liu, Y. Li, K. Yang, Y. Liu, Y. Dong, L. Dong, and E. X. Wu, "M4raw: A multi-contrast, multi-repetition, multi-channel MRI k-space dataset for low-field MRI research," *Sci. Data*, vol. 10, no. 1, p. 264, 2023.



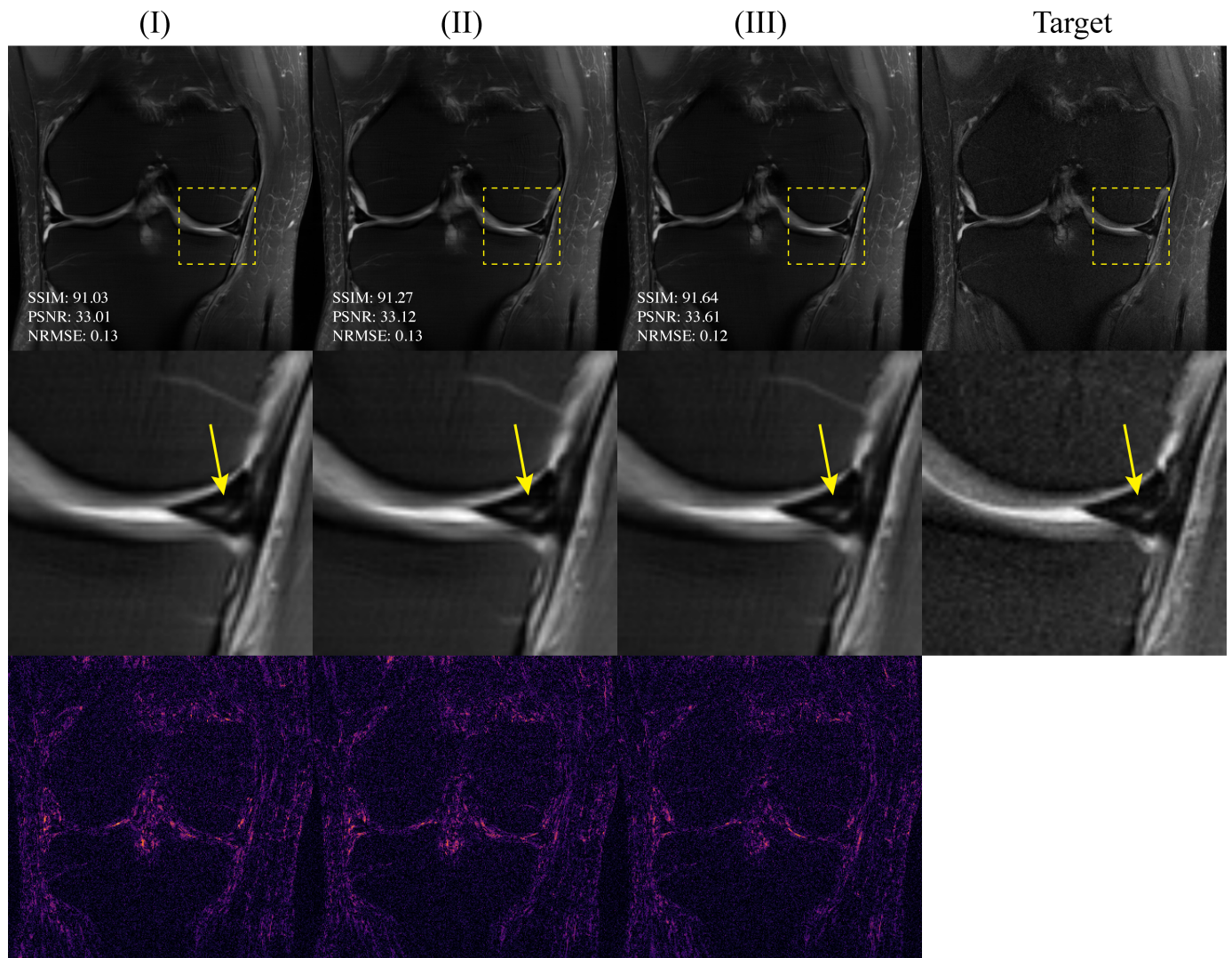
Suppl. Fig. 1: **Quantitative evaluation results in terms of SSIM, PSNR, and NRMSE over the test dataset for Ablation Study A.** Each blue point has x- and y-coordinates representing values achieved by TGVN without and with the proposed projector, respectively. The ideal scenario is that for all samples in the test dataset, the proposed projector leads to better scores (i.e., the blue points are always above the $y = x$ line for SSIM and PSNR, and always below the $y = x$ line for NRMSE). TGVN achieves **better** performance for **almost all** slices in the test dataset.



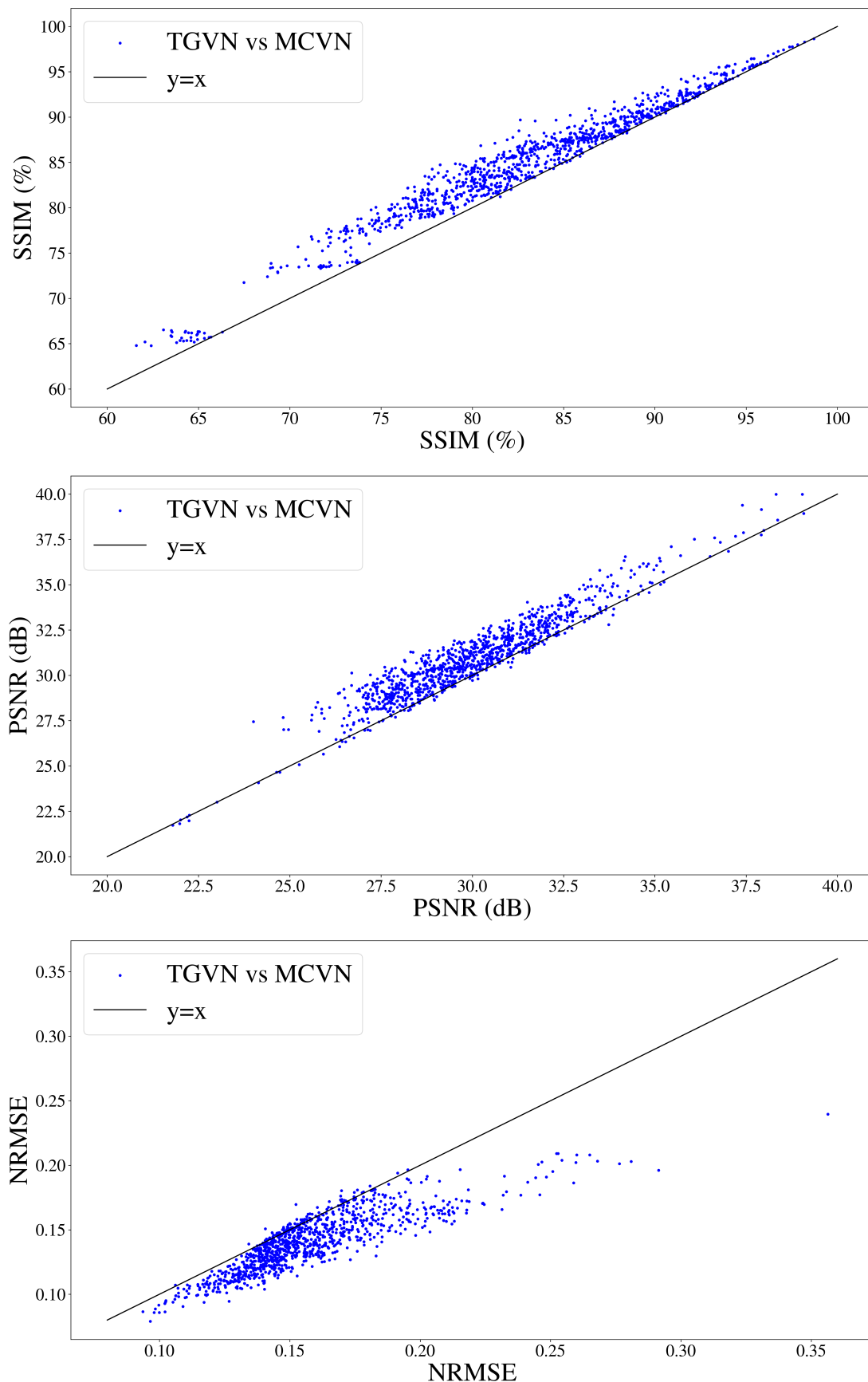
Suppl. Fig. 2: **Representative reconstructed images for Ablation Study B.1.** Left: Target image. (1): Reconstruction using TGVN trained with registered side information, encountering registered side information during inference. (2): Reconstruction using TGVN trained with augmentations simulating misregistrations, encountering misregistered side information during inference. (3): Reconstruction from E2E-VarNet without access to side information. Right: Misregistered side information. The most prominent differences are located inside the dashed yellow boxes. **Despite randomly misregistered side information, (2) preserves anatomical details much better than (3).**



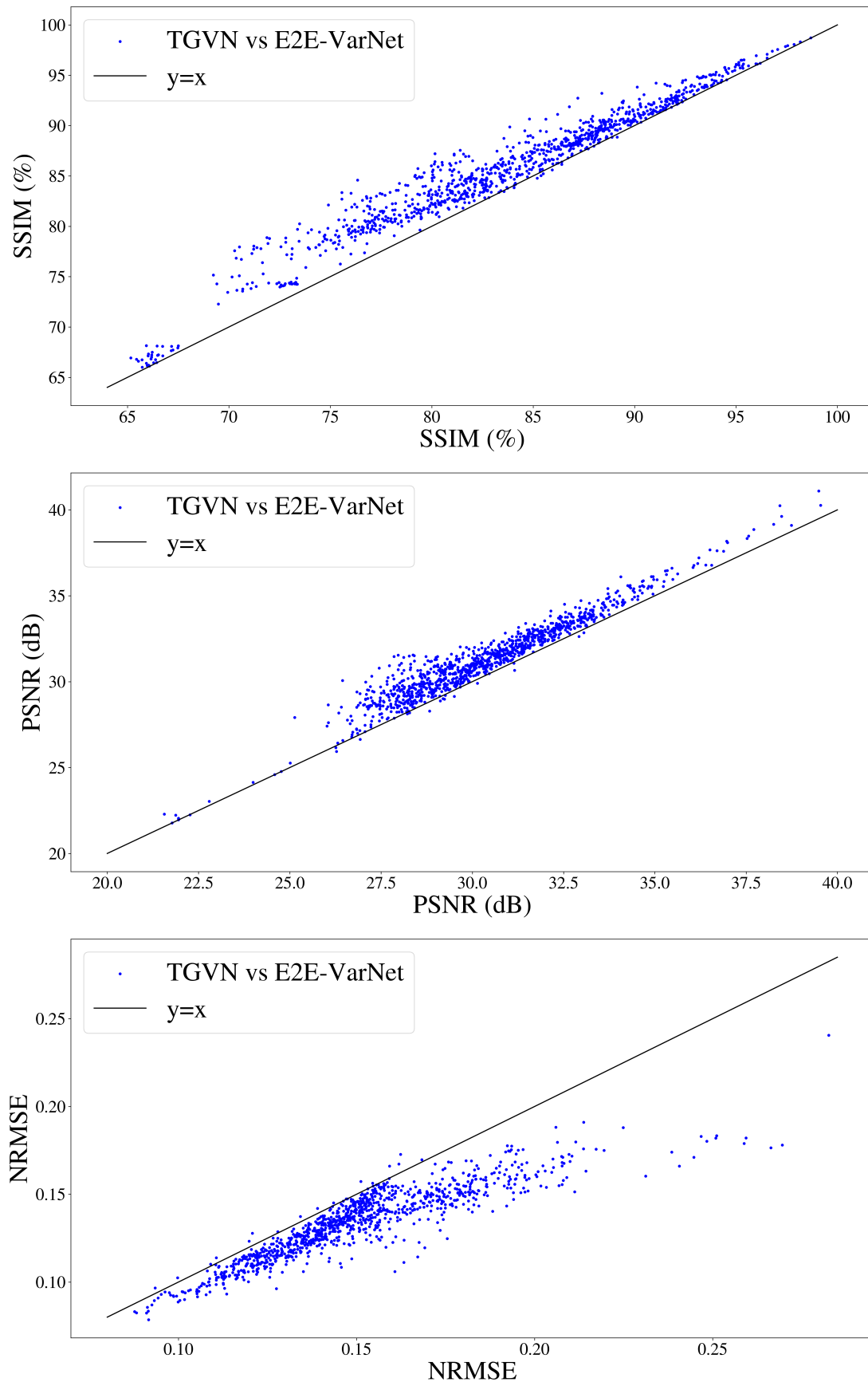
Suppl. Fig. 3: **Quantitative evaluation results in terms of SSIM, PSNR, and NRMSE over the test dataset for Ablation Study B.1.** Each blue point has x- and y-coordinates representing values achieved by E2E-VarNet without side information and TGVN encountering randomly misregistered side information during training and inference, respectively. The ideal scenario is that for all samples in the test dataset, TGVN leads to better scores despite **randomly misregistered side information** (i.e., the blue points are always above the $y = x$ line for SSIM and PSNR, and always below the $y = x$ line for NRMSE). TGVN achieves **better** performance for **almost all slices** in the test dataset.



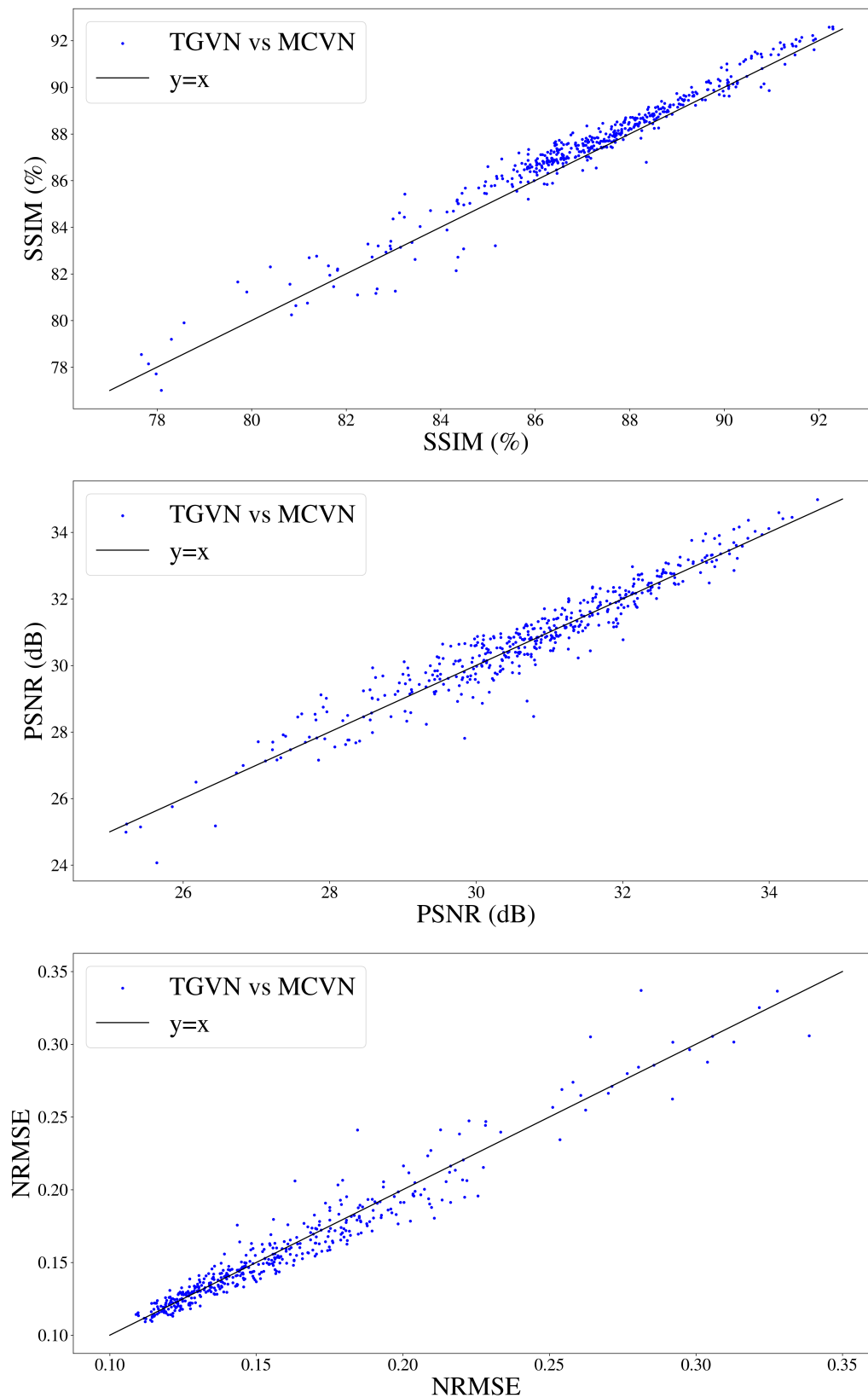
Suppl. Fig. 4: **Representative reconstructed images for Ablation Study B.2.** (I): Reconstruction using TGVN trained with $3\times$ under-sampled side information. (II): Reconstruction using TGVN with $3\times$ under-sampled side information, which is first reconstructed with an E2E-VarNet. (III): Reconstruction using TGVN trained with fully-sampled side information. While the performance metrics differ slightly, the *meniscus tear*, illustrated with yellow arrows, is visible in all reconstructions.



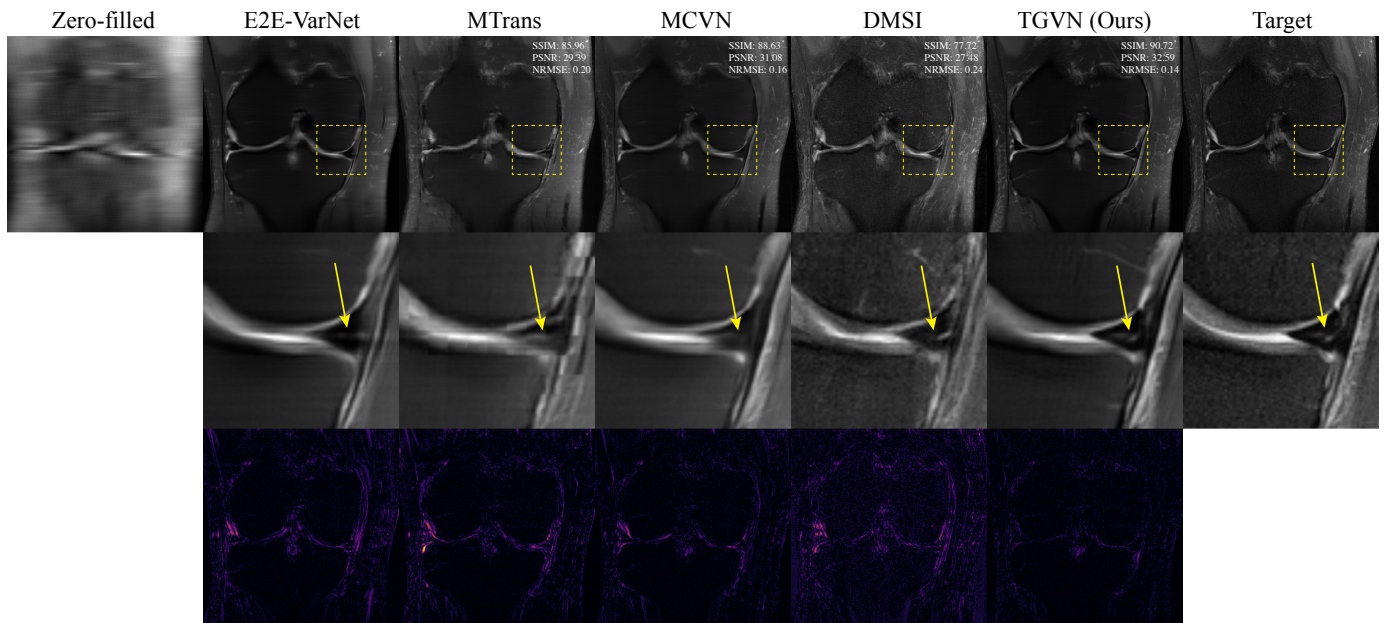
Suppl. Fig. 5: **Quantitative evaluation results in terms of SSIM, PSNR, and NRMSE over the test dataset for Set I.** Each blue point has x- and y-coordinates representing values achieved by MCVN (the second-best performing baseline method) and TGVN, respectively. The ideal scenario is that for all samples in the test dataset, TGVN achieves better scores (i.e., the blue points are always above the $y = x$ line for SSIM and PSNR, and always below the $y = x$ line for NRMSE). TGVN achieves **better** performance for **almost all slices** in the test dataset.



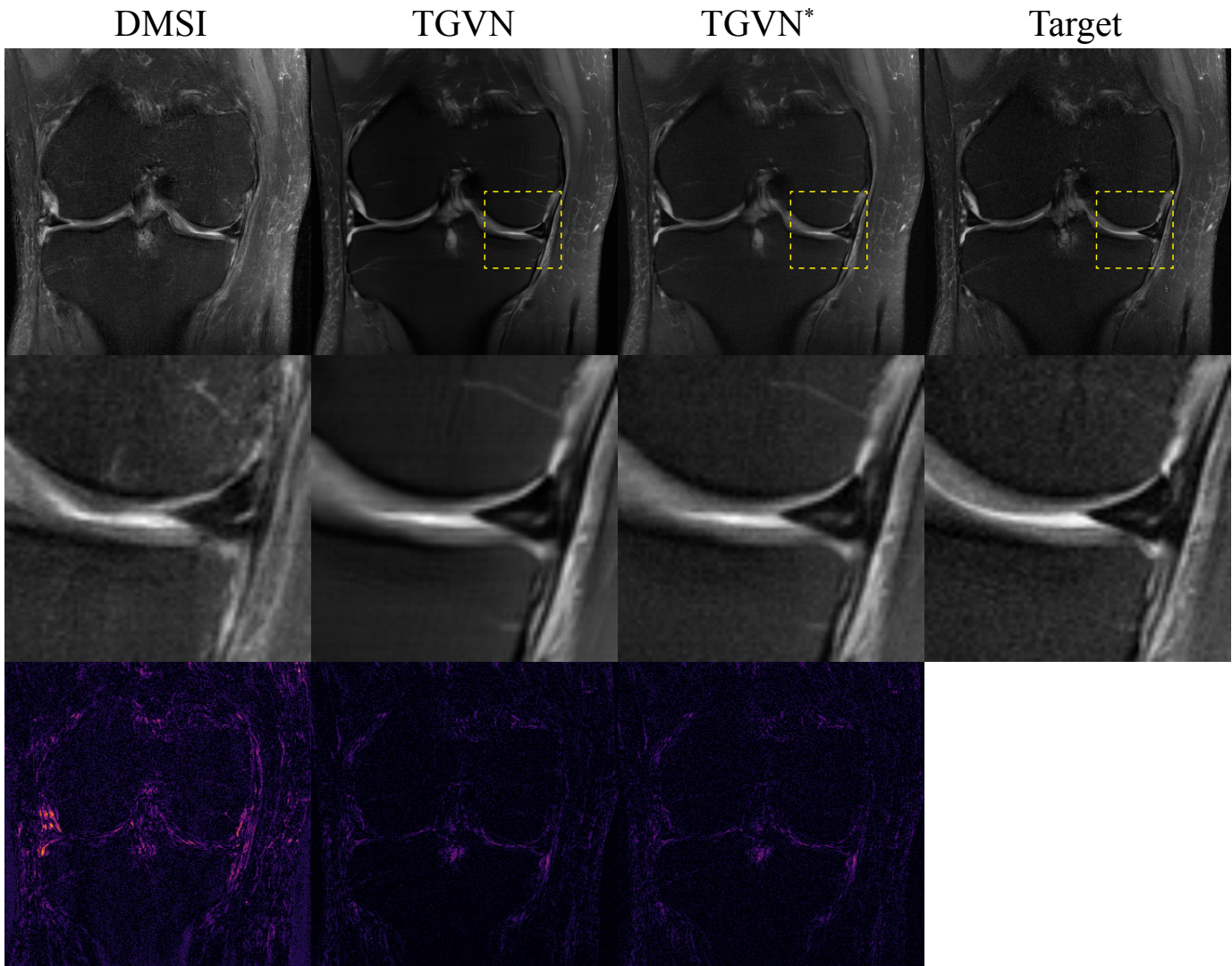
Suppl. Fig. 6: **Quantitative evaluation results in terms of SSIM, PSNR, and NRMSE over the test dataset for Set II.** Each blue point has x- and y-coordinates representing values achieved by E2E-VarNet (the second-best performing method) and TGVN, respectively. The ideal scenario is that for all samples in the test dataset, TGVN achieves better scores (i.e., the blue points are always above the $y = x$ line for SSIM and PSNR, and always below the $y = x$ line for NRMSE). TGVN achieves **better** performance for **almost all slices** in the test dataset.



Suppl. Fig. 7: **Quantitative evaluation results in terms of SSIM, PSNR, and NRMSE over the test dataset for Set III.** Each blue point has x- and y-coordinates representing values achieved by MCVN (the second-best performing method) and TGVN, respectively. The ideal scenario is that for all samples in the test dataset, TGVN achieves better scores (i.e., the blue points are always above the $y = x$ line for SSIM and PSNR, and always below the $y = x$ line for NRMSE). In this case, the PSNR and NRMSE plots are visually closer than the SSIM plots. However, Wilcoxon signed-rank tests still reject the null hypothesis with p -values less than 7×10^{-4} in each case, **demonstrating statistically significant improvements with TGVN.**



Suppl. Fig. 8: **Additional knee image reconstructions from Set I showing the effectiveness of TGVN in leveraging side information.** TGVN is able to reconstruct a high-quality image even at challenging acceleration levels of $20\times$, in comparison to various baselines. The *meniscus tear*, illustrated in the ground truth image and reconstructions with a yellow arrow, is notably more visible in the TGVN reconstruction than in baseline reconstructions. **Top:** Full field of view images. **Middle:** Zoomed-in regions indicated by dashed yellow boxes in the top row. **Bottom:** Absolute differences between each reconstruction and the ground truth, with a consistent color mapping to highlight error magnitudes. TGVN has the smallest error.



Suppl. Fig. 9: **Selected knee image reconstructions from the same subject shown in Suppl. Fig. 8, including TGVN with added image noise.** A common challenge in end-to-end reconstructions compared to generative approaches such as DMSI is a residual smoothing of fine image features or background textures. To enhance the subjective perception of sharpness in images, known as acutance in photography, low levels of Gaussian noise were added back to the reconstructed TGVN output, which is represented as TGVN*. Improved preservation of key features may be appreciated in the TGVN* reconstruction as compared with the DMSI reconstruction.